Transfer-print integration of GaAs p-i-n photodiodes onto silicon nitride waveguides for near-infrared applications

JEROEN GOYVAERTS,[1,2,4,*] SULAKSHNA KUMARI,[1,2,4] SARAH UVIN,[1,2] JING ZHANG,[1,2] ROEL BAETS,[1,2] AGNIESZKA GOCALINSKA,[3] EMANUELE PELUCCHI,[3] BRIAN CORBETT,[3] AND GÜNTHER ROELKENS[1,2]

[1] *Photonics Research Group, Ghent University-imec, Technologiepark 126, 9052 Gent, Belgium*
[2] *Center for Nano- and Biophotonics, Ghent University, Belgium*
[3] *Tyndall National Institute, University College Cork, Lee Maltings, Cork, Ireland*
[4] *Contributed equally*
jeroen.goyvaerts@ugent.be

Abstract: We demonstrate waveguide-detector coupling through the integration of GaAs p-i-n photodiodes (PDs) on top of silicon nitride grating couplers (GCs) by means of transfer-printing. Both single device and arrayed printing is demonstrated. The photodiodes exhibit dark currents below 20 pA and waveguide-referred responsivities of up to 0.30 A/W at 2V reverse bias, corresponding to an external quantum efficiency of 47% at 860 nm. We have integrated the detectors on top of a 10-channel on-chip arrayed waveguide grating (AWG) spectrometer, made in the commercially available imec BioPIX-300 nm platform.

1. Introduction

Over the last few years, the field of silicon nitride (SiN_x) photonic integrated circuits (PICs) has gained a lot of interest due to a variety of material properties of SiN_x [1–3]. The lower index contrast of SiN_x with silicon oxide (SiO_x) compared to silicon also results in lower propagation losses and lower mode confinement for sensing applications [4]. The broad transparency window opens up the field of visible light photonics down to 450 nm [5], while the lower two-photon absorption coefficient is relevant for applications in the field of non-linear optics, such as frequency comb generation [6]. Another important property is the low temperature deposition process of plasma-enhanced chemical vapor deposition (PECVD) nitride, allowing co-integration with complementary metal-oxide semiconductor (CMOS) electronics [5].

As such, academic and commercial interest in SiN_x has been growing in Europe. There are several commercially available SiN_x offerings in multi-project wafer (MPW) mode, such as imec's BioPIX 300 nm thick PECVD SiN_x. Other foundries, such as Lionix, Ligentec and CSIC-CNM offer low pressure chemical vapor deposition (LPCVD) nitride from 150 nm up to 800 nm thickness. As the platforms mature, additional functionality is being added besides the commonly available heaters/phase shifters. Recently, Lionix demonstrated the co-integration of an InP gain chip for 1550 nm through butt-coupling [7] and Ligentec showed wafer-bonding-based integration of PDs for 1550 nm as well [8]. However, a lack of integrated light sources and detectors remains for wavelengths other than the telecom range. This hinders the current deployment and application range of the SiN_x PICs. Hybrid integration of III-V active components, for instance the butt-coupled InP gain chip, offers a solution for more advanced SiN_x PICs. There are several approaches for hybrid and heterogeneous integration, such as flip-chipping, butt-coupling, die- or wafer-bonding, hetero-epitaxial growth and, more recently, micro-transfer-printing (muTP). Wafer-to-wafer bonding is a well-known approach for integrating III-V devices in the telecom
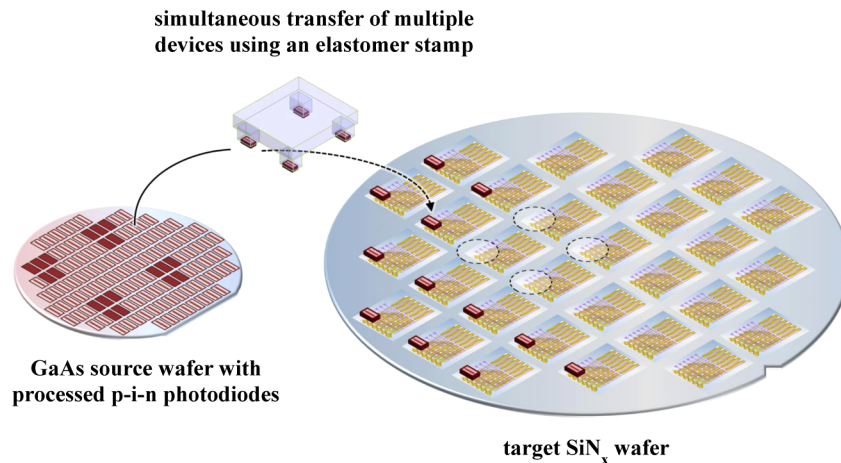
Fig. 1. Concept illustration of the wafer-scale compatible micro-transfer-printing technology, where III-V components such as photodiodes are transferred from the III-V source substrate to a SiN$_x$ photonics wafer in a parallel manner.

wavelength range. While the technique is wafer-scale compatible, it does not make efficient use of the more expensive III-V wafer by etching away most of the III-V wafer after bonding. The technique also requires III-V processing to be done on top of the circuit wafer. As the current SiN$_x$ market is still developing and the application demonstrators are still in the low volume range, the techniques of choice, so far, have been flip-chipping or butt-coupling active components [9]. The downside is that those approaches do not offer a route to scaling towards high-volume or to the dense integration of active components in a cost effective manner.

We believe that the heterogeneous integration by means of muTP, as illustrated in Fig. 1 is the best candidate to integrate III-V active components and solve the aforementioned bottlenecks. With this technique, coupons are pre-fabricated on a source substrate, here p-i-n PDs on a GaAs substrate. These devices are tethered to the substrate with an anchoring layer, and subsequently released with an underetch of the device layers. Afterwards, a polydimethylsiloxane (PDMS) stamp is used to pick-up the coupons. The stamp touches down on the coupons, and tears off the coupons by breaking the anchors through a rapid upward motion. Following this, the devices are transferred and printed onto a target substrate, here a silicon nitride PIC. Earlier demonstrations have proven the viability of this technique on grating-assisted III-V photodetectors [10,11] for other wavelengths. For such grating assisted devices, the performance is strongly related to the performance and directionality of the underlying GC and the epitaxial layer structure of the PD. Previously, we have reported on a transfer-printed GaAs MSM photodetector for high speed applications, with a typical responsivity of 0.1 A/W and 40 Gbit/s operation [12]. The key advantages that muTP brings to photodetector integration, is that it is a cost effective and wafer-scale compatible process. High throughput is achieved by printing arrays of devices in a massively parallel fashion. It makes more efficient use of its source material (here, III-V) in comparison to wafer-bonding. For wafer bonding approaches, the alignment between III-V and SiN$_x$ is defined by the accuracy of the lithography step. Given the nature of the pick-and-place method of muTP, a degree of uncertainty is introduced with the alignment accuracy of the printing step. The X-Celeprint advertised specification of ± 1.5 mum −3σ [13] more than suffices for grating-assisted photodetectors, as will be detailed in the following section. muTP is also not limited to a specific material platform, as is the case for hetero-epitaxial growth. Various material systems, such as GaAs, GaN, InP, GaSb, Si and others can be integrated.

In this work, GaAs is the material of choice due to its operation in the near-infrared with relevant applications ranging from datacom links to photonic interposers and, more recently, in biosensing. The integration of a GaAs half-VCSEL on top of a SiN$_x$ photonic circuit has already been demonstrated using adhesive bonding and offers a low-power-consumption single-mode light source on-chip [14]. The possibility of having an integrated light source and integrated detectors on-chip will open up a range of bio-related applications, such as Optical Coherence Tomography (OCT) [15], on-chip Raman spectroscopy [16–18] and refractive index sensing of bio-markers through an on-chip AWG spectrometer [19–21]. In this work, we demonstrate the integration of GaAs p-i-n photodetectors on the imec BioPIX platform by means of µTP. We prove their relevance for sensing applications by integrating them on top of the output GCs of the channels of an on-chip AWG spectrometer. We detail the design of the epitaxial layers, the grating coupler parameters and the photonic circuit. We also cover the photodetector fabrication and transfer-printing process. Finally, we present the measurement results for individually characterized PDs and for those printed onto the on-chip spectrometer demonstrator.

2. Design

The GaAs p-i-n detector is integrated onto a silicon nitride waveguide circuit by printing it on top of a grating coupler, as shown in Fig. 2(a). The waveguide optical power is diffracted upwards through the grating coupler, towards the bottom surface of the detector. The p-i-n detector is a vertical device with a transparent n-contact layer at the bottom, which is shown in blue in Fig. 2(a). The intrinsic GaAs, shown in red, is the absorbing layer and encompasses the main mesa with length L_M and width W_M. In reality, the surface area of the main mesa slightly extends over the surface area of the GC. This is chosen to relax the alignment restrictions over the capabilities of the tool. The p-contact layer on top, shown in yellow, has a distinct tetris-shape p-metal contact that acts as a pattern recognition marker to help with alignment during the printing process. The following paragraphs detail the p-i-n layerstack design, the GC design and the PIC design.
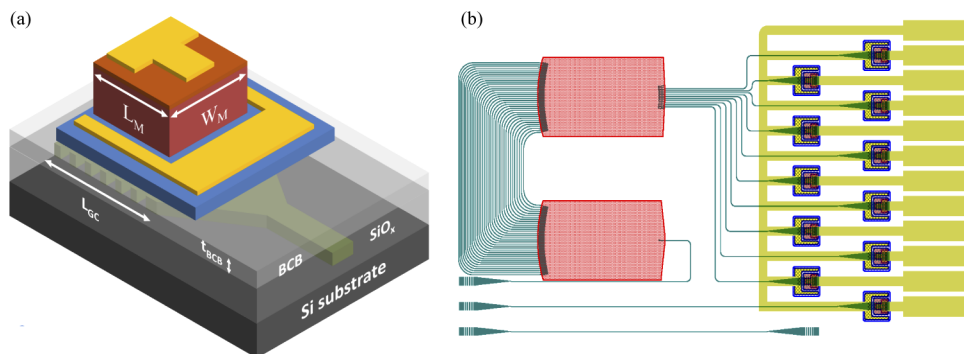

Fig. 2. (a) 3D model of the p-i-n photodiode on top of a SiN$_x$ GC, showing the relevant design parameters and (b) a GDSII schematic of the on-chip spectrometer with printed PDs onto the output GCs.

The epitaxial layer stack of the photodiodes is listed in Table 1. The top InAlP layer is a sacrificial layer to prevent oxidation prior to processing. The device layers (from top to bottom) start with a 300 nm thick, p-doped GaAs layer, followed by the intrinsic GaAs absorption layer. The typical absorption coefficient of GaAs in the wavelength range of 750 nm - 855 nm is 1.7 µm^{-1} - 1.2 µm^{-1}. Therefore, the absorption layer is chosen sufficiently thick at 2 µm. The fraction of light that is not absorbed initially, will reflect at the p-contact and travel again through the absorption layer. The amount of light that is absorbed over the amount of light that enters the

PD is defined here as the internal quantum efficiency in Eq. (1). The value is close to unity and ensures a high responsivity for the devices.

Table 1. III-V photodetector epitaxial layer stack

Layer no.	Type	Material	Thickness [nm]	Doping [cm^{-3}]	Dopant
6	Protection	$In_{0.49}Al_{0.51}P$	500	NID	-
5	P-Contact	GaAs	300	$5 \cdot 10^{19}$	C
4	Absorption	GaAs	2000	NID	-
3	N-Contact	$Al_{0.15}Ga_{0.85}As$	600	$3 \cdot 10^{18}$	Si
2	Etch Stop	GaAs	4	NID	-
1	Release	$In_{0.49}Al_{0.51}P$	1000	NID	-
0	Substrate	GaAs	-	NID	-

The n-doped contact layer below the absorption layer is an $Al_{0.15}Ga_{0.85}As$ layer with a bandgap wavelength of 760 nm. This ensures the transparency of the n-contact layer. The n-contact layer is 600 nm thick, which facilitates the processing of the coupons. Underneath the n-contact layer is a thin 4 nm GaAs etch stop layer that ensures optimal etch selectivity and has only a minimal impact on the responsivity. For GaAs material systems, there are three likely candidates for the release layer: InAlP, InGaP and high aluminium containing $Al_xGa_{1-x}As$ ($x>0.90$). As demonstrated by Tyndall [22], InAlP is the most suited choice for releasing thin film membranes with respect to etch selectivity and ease of processing.

$$IQE = \frac{Light\ absorbed\ by\ PD}{Light\ coupled\ into\ PD}$$
$$= 1 - e^{-\alpha \cdot t} \tag{1}$$
$$\geq 0.95$$

The wavelength range of interest for this work is 760 nm to 870 nm, which is covered by imec's BioPIX 300 nm platform. The platform consists of a single PECVD nitride layer, which is 300 nm thick. The bottom oxide thickness is 3.3 μm, while the top oxide is 2 μm thick. There are two etch steps available, a 150 nm half etch and a 300 nm full etch. Grating couplers can be fabricated in either the half etch or full etch step. The half etch gratings have a lower grating strength, but a higher upward directionality. The full etch gratings, on the other hand, have a higher grating strength but a lower upward directionality due to its symmetry. Given that the standard single-mode fiber for the NIR region has a core diameter of 4.6 μm, a typical grating coupler has a 5 μm by 5 μm surface area and uses the full etch grating to diffract as much light as possible over the 5 μm. PDs are however not limited to the same mode-size restriction as single-mode fibers. Therefore, the length of the grating of the PD-on-GC system was increased to 15 μm, while the width was kept at 5 μm.

The mesa dimensions L_M and W_M of the PD were selected at 25 μm by 25 μm, accommodating to the larger gratings and thus collecting more light than what is possible with a SMF. The overdimensioning of the PDs with respect to the GC gave a large sideways misalignment tolerance of 10 μm and an on-axis misalignment of 5 μm in each direction. This is far more than the misalignment of the transfer-printer tool.

Given that the wavelength region is too broad to be covered by a single grating, both the full etch and the half etch grating are used. The GC for the 760 nm to 800 nm range is a uniform, full etch grating with a 50% fill factor (FF) and a 0.57 μm pitch. The second GC is a uniform, half etched grating with a 50% FF and a 0.59 μm pitch for the 810 nm to 870 nm range. The fiber-interfacing configurations of those GCs have a measured insertion loss of -7.8 and -9 dB per GC, respectively. The coupling efficiency of the larger gratings towards the GaAs PD is

simulated in a Lumerical FDTD 2D cross sectional model. The WG-to-PD coupling efficiencies, $\eta_{WG-to-PD}$, are 44% for the full etch grating centered around 780 nm and 56% for the half-etch grating centered around 850 nm. The overall efficiency of the PD-on-GC system is defined here as the external quantum efficiency and relates the light inside the waveguide to the amount of light that is absorbed by the PD, as given in Eq. (2).

$$EQE = \frac{Light\ absorbed\ by\ PD}{Light\ inside\ WG}$$
$$= \eta_{WG-to-PD} \cdot IQE$$
$$\approx \eta_{WG-to-PD}$$

(2)

In terms of PIC design, three circuits are designed, as illustrated in Fig. 2: a PD-on-GC test site for the 780 nm range and one for the 850 nm range, consisting of reference gratings and PD transfer-print sites to derive the waveguide-referred responsivity of the devices. A third circuit is the arrayed waveguide grating spectrometer, designed at 780 nm. The AWG is designed using the Luceda filter toolbox [23], making use of the full etched and half etched waveguides of the BioPIX platform. The half etched rib waveguide reduces phase errors in the delay lines of the design. It is a 10 channel spectrometer, with a 1 nm channel width, a 2 nm channel spacing and a FSR of 30 nm. The AWG output channels were distributed to a set of output grating couplers with the same pitch on the PIC (125 μm) as for the PDs on the source substrate. This design thus allows for arrayed PD printing using a multi-post stamp.

3. Fabrication

The PD devices, also referred to as coupons, are defined almost entirely on the native GaAs source substrate, with minor post-processing done after transfer-printing. The process flow is summarized in Fig. 3. The processing on the GaAs source substrate starts with the removal of the InAlP protection layer. The InAlP layer is easily removed by wet etching with a HCl based etchant [24]. In the next step, the p-contact is defined. Just prior to the Ti/Au metal deposition, a quick dip into a 1:1 HCl:DI water solution removes any native oxide on top of the p-contact layer, thus lowering the resistance. Following this, a SiN$_x$ hard mask is deposited and patterned to define the main mesa with an inductively coupled plasma (ICP) dry etch. By monitoring the etch depth with an interferometic profilometer inside the ICP tool, the etch is stopped once the n-GaAs layer is reached. Then, another SiN$_x$ layer is deposited to passivate the sidewalls of the main mesa. This passivation mask is patterned to open up the n-contact layer. Afterwards, the n-contact is formed by depositing a Ni/Ge/Au/Ti/Au contact. In the next step, a second mesa is defined to reach the release layer. A selective wet etch is used for this second mesa, as an over-etch into the release layer will result in the encapsulation and tethers sticking out below the bottom surface of the coupon. This can impede the printing process, resulting in a lower printing yield. Therefore, a wet etch using 5:1 citric acid:H$_2$O$_2$ removes the remaining n-contact Al$_{0.15}$Ga$_{0.85}$As and the GaAs etch stop layer as well, ensuring a smooth interface. The release layer is then patterned with a 1:5 HCl:DI water solution, with an approximate etch rate of the InAlP release layer of 400 nm/minute. With the same mask pattern, the substrate is etched for an additional 100-200 nm, to ensure that the tethers adhere to the GaAs substrate and remove any possible remaining InAlP sacrificial layer between the tethers and the substrate, as shown in Fig. 3(b). Prior to defining the tethers with a Ti-35 photoresist (PR) encapsulation as shown in Fig. 3(c), a short 1:5 HCl:DI water dip is done to remove any native oxide on the GaAs substrate that may have grown in between the processing steps.

After hard baking the photoresist tethers, the devices are ready to be released. Using a 1:1 HCl:DI water solution, an approximate etch duration of 30 minutes is required to release all devices, as represented in Fig. 3(d). After removing the sample from the etchant beaker, the
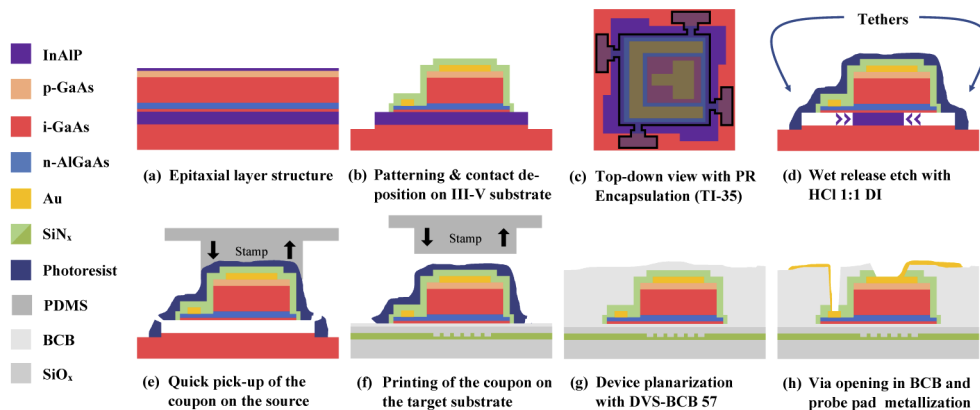
Fig. 3. Schematic of the process flow with (a) the epitaxial layer stack and (b) the patterned device on the source substrate. The release layer is patterned to access the substrate. (c) Shows a top-down view of the photoresist encapsulation in contour that anchors the device to the substrate. The devices are released with an underetch in (d). Afterwards, the devices are picked up with a PDMS stamp in (e) and printed on the SiN$_x$ target PIC in (f). On the target wafer, the encapsulation is removed and the devices are planarized with DVS-BCB in (g) and interconnected in (h).

sample is not rinsed but dipped in several beakers of DI water, to avoid any accidental damage to the fragile tethers. Afterwards, the substrate is left to dry in a wet bench for approximately 30 minutes to allow the remaining fluids in between or below the coupons to evaporate. The devices are then ready for transfer-printing and are loaded in a X-Celeprint μTP-100 sample-scale lab printer for printing the PDs onto the silicon nitride PICs. Pattern recognition markers are defined both on the coupon and the target substrate. For the coupon, the p-contact is shaped in a tetris-like T-block as shown in Fig. 2(a), while quarter-circle markers are defined on the target substrate. The alignment with the pattern recognition markers is visualized in the microscope images of Fig. 4(d) and Fig. 4(e). Prior to loading the substrates onto the transfer-printer, the target die is spin coated with diluted DVS-BCB 35 to achieve a target thickness of approximately 1 μm. Given that the PDs are surface illuminated through a GC, in contrast to adiabatically coupled structures such as transfer-printed DFB lasers [25], the narrow thickness constraint of the DVS-BCB bonding layer is alleviated. A pre-cure of the DVS-BCB on the target substrate is done for the thicker DVS-BCB bonding layer to avoid any lateral shift of the devices during the full-cure step after printing.

As mentioned in section 2., there are three circuit designs on which the coupons were printed: the GC$_{in}$ - GC$_{out}$ test structures for PD characterization at 780 nm and 850 nm and the 10-channel spectrometer at 780 nm. For the multi-channel spectrometer, a multi-post stamp was used to print an array of up to 8 PDs in a single print. The target substrate was designed with the same pitch (125 μm) between the output grating couplers as that of the PDs on the source substrate. Figures 4(d), 4(e) and 4(f) show an array of PDs on the stamp after pick-up, the alignment procedure prior to printing at a 100 μm above the target substrate and the finalized multi-channel output AWG with accompanying pattern recognition structures next to those output gratings.

After transfer-printing, the photoresist encapsulation is first reflown at 135°C for 10 minutes, after which it is removed with a oxygen-plasma reactive ion etch (RIE). Afterwards, the underlying DVS-BCB bonding layer is fully cured at 250°C for 3 hours [26]. In the next step in Fig. 3(g), the devices are all passivated by spin coating a thick DVS-BCB 57 layer and full-curing that as well. Following this, the passivation layer is thinned down to just above the p-contact. Then, sloped VIAs are defined in the BCB using AZ 9260 photoresist that is baked for 2 minutes at 120°C to
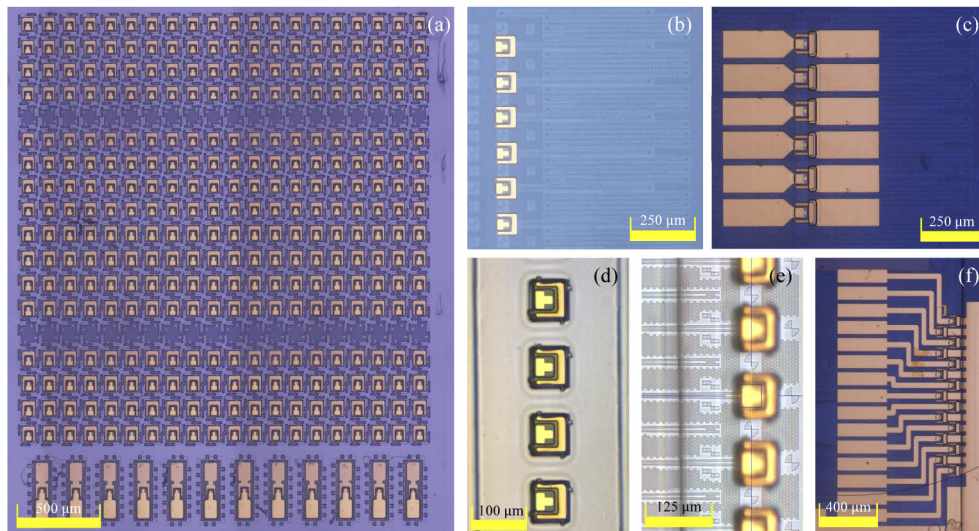
Fig. 4. Microscope images of (a) source substrate with dense PD configuration, a target test site with printed PDs after PR removal in (b) and after post-processing in (c). (d)-(e)-(f) shows the process of arrayed transfer-printing, where a set of PDs is printed in one go, on top of the AWG output channels and interconnected in post-processing.

achieve a 45°sidewall angle. The VIA pattern is transferred from the photoresist into the BCB layer during the RIE etching. An additional SiN$_x$ etch is done to remove any of the remaining passivation layers on top of the metal contacts of the coupon. The final step shown in Fig. 3(h) is the definition of the probe pad metal, which is a combination of Ti/Au on top of the contact metals that are already present on the coupon.

4. Results

The devices were characterized with a broadband Ti-Sapph tunable laser (M2 SolsTis), covering a wavelength range from 760 nm to 900 nm. Due to a laser instability between 802 nm and 808 nm, a 10 nm gap is omitted in the characterization. As a result, the 780 nm-PD is characterized between 760 nm and 800 nm, while the 850 nm-PD is characterized between 810 nm and 900 nm. The wavelength was monitored at the laser system with a high resolution wavelength meter (High Finesse WS7). The resolution of the measurement scans was limited to 2 nm for PD characterization and 0.01 nm to interrogate the AWG channels of the demonstrator. One percent of the laser output power is tapped off and monitored with an external HP power meter (model 81530A) through a 99-1 fiber splitter. A Keithley 2400A voltage-current source-meter is used to reverse bias the PD, while measuring the photocurrent. The dark current was measured with a Keithley 2450 model. The latter device is able to measure a leakage current down to 5 pA. A polarization controller is used before the chip to couple in TE-polarized light. The system has only been studied for this polarization state.

The electrical measurements are performed at room temperature and are summarized in Fig. 5. From the V-I measurements graph Fig. 5(a), one can see the averaged differential series resistance converging to a value of 42 Ohm, with a standard deviation of 7 Ohm. The dark currents for a selection of devices are shown in the histogram in Fig. 5(b). The average of this dark current is 11.48 pA or 1.84 μA· cm^{-2}, with a standard deviation of 4.49 pA or 0.72 μA· cm^{-2}. The dark current is very low for an integrated III-V photodiode [27,28], due to the larger bandgap of GaAs. Nevertheless, the dark current of the devices are on par or lower than that of commercial

solutions [29]. The graphs in Fig. 5(c)-(d) show the I-V curves for different optical intensities in the waveguide. The photocurrents correspond to a single laser line, respectively at 780 nm and 850 nm.
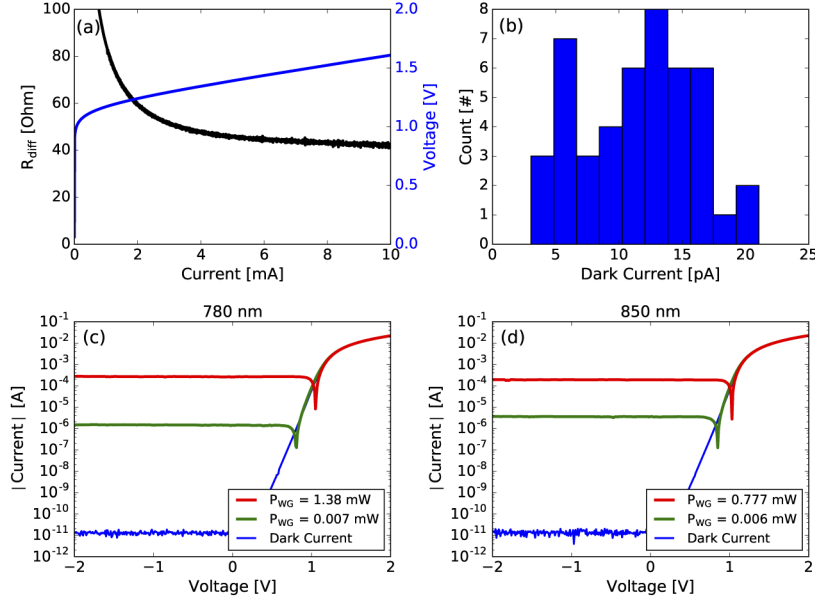

Fig. 5. The electrical performance of the PDs with (a) V-I curve and differential series resistance up to 10 mA, (b) a distribution of the measured dark current at -1V reverse bias, (c) the I-V curves for a PD-on-GC illuminated at 780 nm and (d) at 850 nm.

The responsivity of the PD-on-GC system is defined with respect to the power inside the waveguide, following the reasoning of the EQE. This waveguide-referred responsivity, R_{WG}, is commonly used for integrated PDs [11,30]. R_{WG} is the more relevant figure-of-merit as it includes the coupling scheme and thus better represents a circuit building block. The power inside the waveguide can be derived by adding the insertion loss of the input SMF-GC to the in situ power measurements of the laser. This GC insertion loss was measured on reference GCs just above and below the PD measurement site. The values of these GC reference measurements were averaged into a single spectrum for each wavelength section (780 nm and 850 nm). The corresponding waveguide-referred responsivities are given in Fig. 6(a)-(b). At 0.3 A/W for 850 nm, the obtained waveguide-referred responsivity of the PD-on-GC system is around 21% lower than estimated from simulations as described in Eq. (3) for 850 nm. This can be attributed to a combination of an overestimation of the IQE and a lower coupling efficiency of the GC. The obtained values are around 40% lower than some flip-chip compatible commercial products [29]. It is important to note that the commercial products do not include the WG-to-PD coupling efficiency. The relatively low $\eta_{WG-to-PD}$ is the main reason for the lower R_{WG}. The next steps to improve performance should be directed towards: (a) increasing the amount of scattered light by further increasing the GC length, increasing the amount of upward scattered light by either (b) including a bottom reflector or by (c) increasing the intrinsic directionality of the grating [31].

$$R_{WG,meas} \leq R_{WG,sim}$$

$$\leq \frac{q}{hf} \cdot \lambda \cdot EQE_{sim} \tag{3}$$
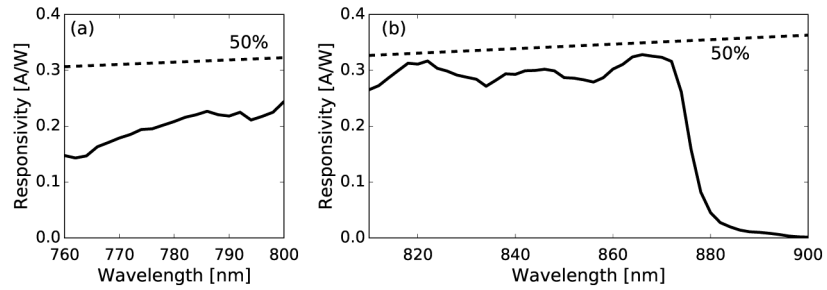
$$0.30[A/W] \leq 0.38[A/W]$$

Fig. 6. The obtained waveguide-referred responsivities for the PD-on-GC system (a) for a grating designed at 780 nm and (b) for a grating designed at 850 nm. The dashed line indicates a 50% external quantum efficiency as a reference for the system performance.
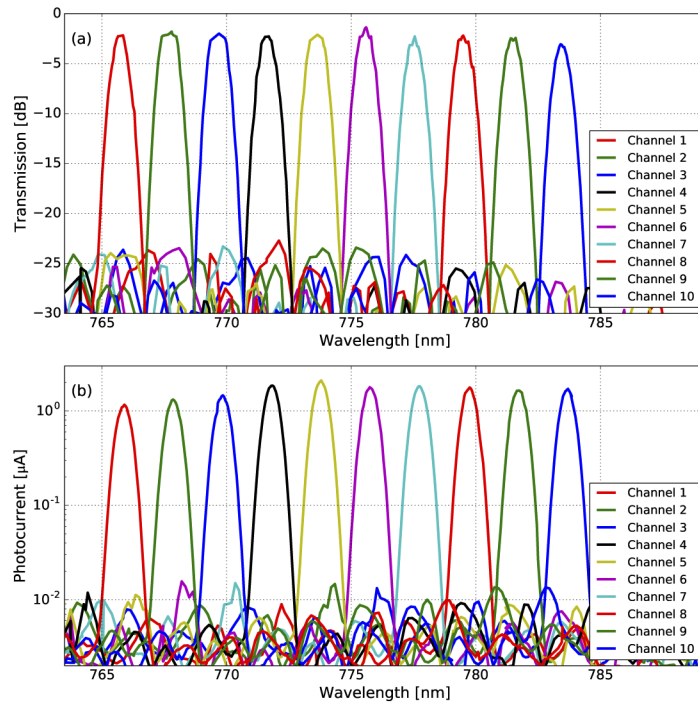

Fig. 7. AWG-demonstrator characterization with (a) measured optical transmission of the 10-channel AWG, (b) the photocurrent of the transfer-printed PDs on top of each channel output grating coupler, measured at -2V reverse bias.

For the AWG characterization, a 10-channel device was designed on the BioPIX platform, with a center wavelength at 780 nm. It can be seen in Fig. 7(a) that the central wavelength is 6.5 nm off-spec. The measurements were done at 11.5 degree fiber angle to compensate for this offset. In Fig. 7(b) the photocurrent measurements are shown, measured at -2 V reverse bias. Both spectra look similar, as the cross-talk characteristics (>20 dB) of the AWG are maintained after printing of the PDs, thus proving the viability of integrated PDs by means of transfer-printing. This circuit closely resembles the on-chip interrogator circuit of the refractive index sensor in [19]. There, the light is similarly outcoupled with a grating coupler and collected off-chip in the far field by a larger CMOS imager sensor. Our proposed solution with integrated GaAs PDs provides an increased responsivity over the silicon imager and allows for further on-chip integration and opens up new application possibilities.

5. Conclusion

We proposed and demonstrated the transfer-printing of GaAs p-i-n photodetectors on top of a commercially available silicon nitride waveguide platform, with coupling enabled by grating couplers. The characteristics of the PD-on-GC system are comparable with off-the shelf commercial products. The measured dark current is in the 15 pA range and the waveguide-referred responsivity of the PD-on-GC system is between 0.2 and 0.3 A/W. The external quantum efficiency is just under 50% near 860 nm, largely limited by the intrinsic lower upward directionality of the single etch grating structures used for coupling the light into the PDs. The benefit of transfer-printing, aside from the large volume-wafer scale compatibility, is that these detectors can be realized on a much smaller footprint compared to commercial flip-chip compatible products. This leads to a significant area decrease and further cost reductions. We have demonstrated this dense integration by parallel transfer printing of arrays of PDs on top of the output channels of an on-chip spectrometer. This work, together with the development on integrated light sources in the NIR region will enable new types of high performing integrated biosensors for future healthcare applications.

Disclosures

The authors declare no conflicts of interest.

References

1. P. Munoz, G. Mico, L. A. Bru, D. Pastor, D. Perez, J. D. Domenech, J. Fernandez, R. Banos, B. Gargallo, R. Alemany, A. M. Sanchez, J. M. Cirera, R. Mas, and C. Dominguez, "Silicon nitride photonic integration platforms for visible, near-infrared and mid-infrared applications," Sensors **17**(9), 2088 (2017).
2. A. Rahim, E. Ryckeboer, A. Z. Subramanian, S. Clemmen, B. Kuyken, A. Dhakal, A. Raza, A. Hermans, M. Muneeb, S. Dhoore, Y. Li, U. Dave, P. Bienstman, N. Le Thomas, G. Roelkens, D. Van Thourhout, P. Helin, S. Severi, X. Rottenberg, and R. Baets, "Expanding the Silicon Photonics Portfolio with Silicon Nitride Photonic Integrated Circuits," J. Lightwave Technol. **35**(4), 639–649 (2017).
3. M. A. Porcel, A. Hinojosa, H. Jans, A. Stassen, J. Goyvaerts, D. Geuzebroek, M. Geiselmann, C. Dominguez, and I. Artundo, "Silicon nitride photonic integration for visible light applications," Opt. Laser Technol. **112**, 299–306 (2019).
4. A. Z. Subramanian, E. Ryckeboer, A. Dhakal, F. Peyskens, A. Malik, B. Kuyken, H. Zhao, S. Pathak, A. Ruocco, A. De Groote, P. Wuytens, D. Martens, F. Leo, W. Xie, U. D. Dave, M. Muneeb, P. Van Dorpe, J. Van Campenhout, W. Bogaerts, P. Bienstman, N. Le Thomas, D. Van Thourhout, Z. Hens, G. Roelkens, and R. Baets, "Silicon and silicon nitride photonic circuits for spectroscopic sensing on-a-chip [Invited]," Photonics Res. **3**(5), B47 (2015).
5. L. Hoffman, A. Subramanian, P. Helin, B. Du Bois, R. Baets, P. Van Dorpe, G. Gielen, R. Puers, and D. Braeken, "Low loss CMOS-Compatible PECVD silicon nitride waveguides and grating couplers for blue light optogenetic applications," IEEE Photonics J. **8**(5), 1–11 (2016).

6. N. Kuse, T. Tetsumoto, G. Navickaite, M. Geiselmann, and M. E. Fermann, "Continuous scanning of a dissipative Kerr-microresonator soliton comb for broadband, high-resolution spectroscopy," Opt. Lett. **45**(4), 927–930 (2020).

7. Y. Fan, J. P. Epping, R. M. Oldenbeuving, C. G. Roeloffzen, M. Hoekman, R. Dekker, R. G. Heideman, P. J. Van Der Slot, and K. J. Boller, "Optically Integrated InP-Si3N4 Hybrid Laser," IEEE Photonics J. **8**(6), 122–123 (2016).

8. Q. Yu, J. Gao, N. Ye, B. Chen, K. Sun, L. Xie, K. Srinivasan, M. Zervas, G. Navickaite, M. Geiselmann, and A. Beling, "Heterogeneous Photodiodes on Silicon Nitride Waveguides with 20 GHz Bandwidth," Opt. Express **28**(10), 14824 (2020).

9. D. Geuzebroek, R. Dekker, and P. van Dijk, "Photonics Packaging Made Visible," Opt. Photonik **12**(5), 34–38 (2017).

10. J. Zhang, A. De Groote, A. Abbasi, R. Loi, J. O'Callaghan, B. Corbett, A. J. Trindade, C. A. Bower, and G. Roelkens, "Silicon photonics fiber-to-the-home transceiver array based on transfer-printing-based integration of III-V photodetectors," Opt. Express **25**(13), 14290 (2017).

11. G. Muliuk, K. Van Gasse, J. Van Kerrebrouck, A. J. Trindade, B. Corbett, D. Van Thourhout, and G. Roelkens, "4 A-25 Gbps polarization diversity silicon photonics receiver with transfer printed III-V photodiodes," IEEE Photonics Technol. Lett. **31**(4), 287–290 (2019).

12. G. Chen, J. Goyvaerts, S. Kumari, J. Van Kerrebrouck, M. Muneeb, S. Uvin, Y. Yu, and G. Roelkens, "Integration of high-speed GaAs metal-semiconductor-metal photodetectors by means of transfer printing for 850 nm wavelength photonic interposers," Opt. Express **26**(5), 6351 (2018).

13. C. A. Bower, M. A. Meitl, S. Bonafede, D. Gomez, A. Fecioru, and D. Kneeburg, "Heterogeneous integration of microscale compound semiconductor devices by micro-transfer-printing," *Proc. - Electron. Components Technol. Conf.* 963–967 (2015).

14. S. Kumari, E. P. Haglund, J. S. Gustavsson, A. Larsson, G. Roelkens, and R. G. Baets, "Vertical-Cavity Silicon-Integrated Laser with In-Plane Waveguide Emission at 850 nm," Laser Photonics Rev. **12**(2), 1700206 (2018).

15. T. van Leeuwen, I. Akca, N. Angelou, N. Weiss, M. Hoekman, A. Leinse, and R. G. Heideman, "On-chip Mach-Zehnder interferometer for OCT systems," Adv. Opt. Technol. **7**(1-2), 103–106 (2018).

16. A. Dhakal, F. Peyskens, S. Clemmen, A. Raza, P. Wuytens, H. Zhao, N. Le Thomas, and R. Baets, "Single mode waveguide platform for spontaneous and surface-enhanced on-chip Raman spectroscopy," Interface Focus **6**(4), 20160015 (2016).

17. H. Zhao, S. Clemmen, A. Raza, and R. Baets, "Stimulated Raman spectroscopy of analytes evanescently probed by a silicon nitride photonic integrated waveguide," Opt. Lett. **43**(6), 1403 (2018).

18. H. Zhao, B. Baumgartner, A. Raza, A. Skirtach, B. Lendl, and R. Baets, "Multiplex volatile organic compound Raman sensing with nanophotonic slot waveguides functionalized with a mesoporous enrichment layer," Opt. Lett. **45**(2), 447 (2020).

19. D. Martens, P. Ramirez-Priego, M. S. Murib, A. A. Elamin, A. B. Gonzalez-Guerrero, M. Stehr, F. Jonas, B. Anton, N. Hlawatsch, P. Soetaert, R. Vos, A. Stassen, S. Severi, W. Van Roy, R. Bockstaele, H. Becker, M. Singh, L. M. Lechuga, and P. Bienstman, "A low-cost integrated biosensing platform based on SiN nanophotonics for biomarker detection in urine," Anal. Methods **10**(25), 3066–3073 (2018).

20. P. Ramirez-Priego, D. Martens, A. A. Elamin, P. Soetaert, W. Van Roy, R. Vos, B. Anton, R. Bockstaele, H. Becker, M. Singh, P. Bienstman, and L. M. Lechuga, "Label-Free and Real-Time Detection of Tuberculosis in Human Urine Samples Using a Nanophotonic Point-of-Care Platform," ACS Sens. **3**(10), 2079–2086 (2018).

21. M. S. Murib, D. Martens, and P. Bienstman, "Label-free real-time optical monitoring of DNA hybridization using SiN Mach-Zehnder interferometer-based integrated biosensing platform," J. Biomed. Opt. **23**(12), 1 (2018).

22. B. Corbett, R. Loi, W. Zhou, D. Liu, and Z. Ma, "Transfer print techniques for heterogeneous integration of photonic components," Prog. Quantum Electron. **52**, 1–17 (2017).

23. L. Photonics, "Filter Toolbox," (2020).

24. C. W. Cheng, K. T. Shiu, N. Li, S. J. Han, L. Shi, and D. K. Sadana, "Epitaxial lift-off process for gallium arsenide substrate reuse and flexible electronics," Nat. Commun. **4**(1), 1577 (2013).

25. J. Zhang, B. Haq, J. O'Callaghan, A. Gocalinska, E. Pelucchi, A. J. Trindade, B. Corbett, G. Morthier, and G. Roelkens, "Transfer-printing-based integration of a III-V-on-silicon distributed feedback laser," Opt. Express **26**(7), 8821 (2018).

26. S. Keyvaninia, M. Muneeb, S. Stanković, P. J. Van Veldhoven, D. Van Thourhout, and G. Roelkens, "Ultra-thin DVS-BCB adhesive bonding of III-V wafers, dies and multiple dies to a patterned silicon-on-insulator substrate," Opt. Mater. Express **3**(1), 35 (2013).

27. K. Sun, D. Jung, C. Shang, A. Liu, J. Morgan, J. Zang, Q. Li, J. Klamkin, J. E. Bowers, and A. Beling, "Low dark current III-V on silicon photodiodes by heteroepitaxy," Opt. Express **26**(10), 13605 (2018).

28. Y. Wan, C. Shang, J. Huang, Z. Xie, A. Jain, and J. Norman, "Low-dark current 1.55 um InAs quantum dash waveguide photodiodes," ACS Nano **14**(3), 3519–3527 (2020).

29. V-I-Systems, "V-I-Systems Optical Chips," (2019).

30. R. Wang, S. Sprengel, M. Muneeb, G. Boehm, R. Baets, M.-C. Amann, and G. Roelkens, "2 μm wavelength range InP-based type-II quantum well photodiodes heterogeneously integrated on silicon photonic integrated circuits," Opt. Express **23**(20), 26834 (2015).

31. Y. Chen, R. Halir, I. Molina-Fernández, P. Cheben, and J.-J. He, "High-efficiency apodized-imaging chip-fiber grating coupler for silicon nitride waveguides," Opt. Lett. **41**(21), 5059 (2016).